Ceramics International 46 (2020) 16770–16780

Contents lists available at ScienceDirect

Ceramics International

journal homepage: www.elsevier.com/locate/ceramint

New dielectric anomalies in the A-site highly deficient Na_xNbO_3 electroceramics

M.L. López[a], I. Álvarez-Serrano[a,*], A. Galdámez[b], E. Rodríguez-Aguado[c], E. Rodríguez-Castellón[c], Y. Saad[d]

[a] Dep. Química Inorgánica, Facultad de Ciencias Químicas, Universidad Complutense de Madrid, 28040, Madrid, Spain
[b] Dep. Química, Facultad de Ciencias, Universidad de Chile, Santiago, Chile
[c] Dep. Química Inorgánica, Facultad de Ciencias, Universidad de Málaga, 29017, Málaga, Spain
[d] Dep. Chimie, Faculté des Sciences, Université de Monastir, 5019, Monastir, Tunisia

ARTICLE INFO

Keywords:
Dielectrics
Sodium niobate
A-site vacancies
PTCR

ABSTRACT

Highly sodium deficient $Na_{0.6}NbO_3$ (NN) ceramics were prepared and characterized. Their mean structure could be described by a mixture of the predominant P polymorph (S.G. *Pbma*) and the Q phase (S.G. $P2_1ma$), at room temperature, as deduced from Rietveld refinements of Powder X-ray diffraction and Raman scattering data. Besides, microstructural and compositional heterogeneity was evidenced from HRTEM and XPS analyses. Dielectric measurements on this highly vacancies-containing NN material indicated a hysteretic transition taking place at ~12 and −18 °C on the heating and cooling regimes, respectively. This means a considerable shift to lower temperatures of the transition temperatures concerning the P/Q transformations previously described for the $NaNbO_3$ material. At an intermediate frequency of 10 kHz, maximum permittivity and tangent loss values of $\varepsilon' = 1250$ and $tg\delta = 2$ were obtained on heating, whereas lower values of $\varepsilon' = 65$ and $tg\delta = 0.04$ were displayed on cooling regime. These anomalies were interpreted in terms of ferrolectric-antiferroelectric-paralectric phase-transitions implying a PTCR behavior within certain temperature range. This response, observed in this complex material for the first time, has interesting implications for the possible application of NN ceramics in sensing and dielectric materials fields.

1. Introduction

Advanced ceramic materials are inorganic, non-metallic materials, which can become active in response to specific requirements according to their properties: thus, electroceramics, magnetoceramics, optoceramics, multiferroics, etc. Among them, several phases as lead-free alkaline niobates stand out for their multifunctional character, which finds potential applications in a wide range of industrial and commercial fields [1]. Particularly, the $NaNbO_3$ (NN) ceramic material and derived phases have been extensively studied since several decades due to their attractive electrical and polarization properties linked to their particular structural characteristics [2]. From the structural point of view, $NaNbO_3$ is a complex system, i.e. it presents up to seven polymorphs depending on different experimental variables [3]. Several structural transitions have been reported for this material as a function of temperature, grain size and particle morphology in nanostructures [4,5]. Moreover, the stabilization of coexistent phases with different symmetries in samples of $NaNbO_3$ has been established from first principle calculations, PDF analysis and neutron diffraction studies [6]. In fact, the thermodynamic stability of several $NaNbO_3$ polymorphs is similar at certain conditions, chemical composition, particle size, etc. At room temperature two polymorphs usually coexist, often referred to as P and Q phases, which correspond to the antiferrolectric (AFE) nonpolar P*bma* and the ferroelectric (FE) polar $P2_1ma$ phases, respectively. Recent efforts have succeeded to synthesize separately single phases of P and Q samples, by means of achieving different nano-morphologies (cube or ribbon-like) [5] and by applying different sintering temperatures [7]. These polymorphs show promising performance for different application fields; thus, P phase is interesting for data storage memories and electromechanical devices, whereas the Q polymorph seems to be more adequate for energy storage as a high-power electrical system, and for photocatalytic processes related to hydrogen evolution [8].

Recently, both the sodium niobate and its derived compounds have attracted renewed interest in the search for new environmentally

* Corresponding author. Dep. Química Inorgánica, Fac. Ciencias Químicas, Univresidad Complutense de Madris, Ciudad universitaria, pza. Ciencias, 28040, Madrid, Spain.
E-mail address: ias@ucm.es (I. Álvarez-Serrano).

https://doi.org/10.1016/j.ceramint.2020.03.253
Received 13 February 2020; Received in revised form 22 March 2020; Accepted 26 March 2020
Available online 28 March 2020

friendly electroceramics. Particularly, NN has attracted much attention due not only to its piezoelectric response but also to its optical [9] and catalytic properties [8,10,11]. As mentioned above, this NN material shows several structural transitions as a function of temperature [12], which can be tuned for optimizing a desired property through different strategies. Thus, tailoring the particle size [4,13], modifying the sintering temperature [7], doping [6,14,15], and applying an electrical field [16]. When controlled adequately, all these conditions permit to modulate the dielectric response [17]. Besides, the stabilization of vacancies at the A-site has been employed as a strategy for tailoring the symmetry of the phases [18] and therefore modulating the conditions of the AFE-FE transitions [19] or, in general, the temperature at which the dielectric anomalies take place.

Among niobium mixed oxides, there are several examples of perovskite-type materials which present high A-site deficiency. In particular, the stable $LaNb_3O_9$ and the metastable $BiNb_3O_9$ phases display a good dielectric behavior. In both cases only one third of the A-sites are occupied. In the Bi-containing material a partial ordering between vacancies and Bi cations has been reported [20]. The dielectric response of $NaNbO_3$–$LaNb_3O_9$ solid solutions has been studied at temperatures above room temperature, showing dielectric maxima around 400 °C and high permittivity values [21].

In FE ceramic materials, particularly $BaTiO_3$ and derived-systems, positive temperature coefficient of resistance (PTCR) phenomenon has been extensively studied [22]. In general, thermistors are temperature-sensing elements, which display a great change in electrical resistance over a small temperature range. PTCR ceramic thermistors not $BaTiO_3$-based are rare in literature. Ferroelectricity in ceramics is usually related to structural transitions between a non-polar phase and a polar one. Several decades ago, the works of Heywang [23] showed that this phenomenon is not observed in single-crystals and in polycrystalline materials the conductivity is controlled by an electrostatic energy ($\sim 1/\varepsilon$) at the grain boundaries. High or low lattice disruptions between domains give rise to a range of barrier potentials between grains in a given sample [24].

Among the different aspects affecting the conductivity in $BaTiO_3$ ceramics, it has been stated that the effects of domain walls within a grain due to structural anisotropy are the main factor [24]. The Heywang model relates the sharp change in resistivity to the sudden increase in ε' at a given temperature, the number of the carriers in the depletion layer and the concentration of acceptor states at the surface [23]. Jonker includes in the model the role of the spontaneous polarization at that given temperature. Furthermore, Kulwicki and Purdes introduce the piezoelectric effect and its effects in the modification of the mentioned parameters. Thus, the compositional and microstructural complexity of the samples leads to a range of resistivity values of the grain boundaries [25]. In this sense, an attempt to model the observed phenomena in our samples should have in mind together all these considerations with a statistical approach. This approach should be able to take into account the high complexity of the microstructural scenario [24].

We previously observed a PTCR behavior near room temperature in stoichiometric ceramics belonging to the $NaNbO_3$–$BiFeO_3$ system, in the context of their dielectric characterization at high temperatures [26]. We have therefore been interested in getting deeper insight about this particular phenomenon displayed by these samples near room temperature.

As mentioned above, the versatility of the perovskite structure permit in some cases to stabilize the $A_{1/3}NbO_3$ composition. Thus, having in mind the ideal $Na_{1/3}NbO_{3-x}$ composition, we have explored the synthesis of possible $Na_{1/3+x}NbO_{3-\delta}$ phases. We found that a perovskite could be stabilized as a single phase for a 0.6Na:1Nb cationic ratio. Thus, in this work we report the preparation and characterization of such $Na_{0.6}NbO_{3-\delta}$ ceramics sintered at different temperatures. In order to analyze this intriguing response in connection with the relevant parameters implied, we carried out a careful structural, compositional, microstructural and electrical characterization.

2. Materials and methods

2.1. Experimental techniques

Powder X-Ray diffraction (XRD) patterns were registered at room temperature with a XPERT-PRO diffractometer using Cu-Kα radiation (λ = 1.5406 Å). Data were collected in the range $5° \leq 2\theta \leq 120°$ range with a step of 0.0167° and analyzed by the Rietveld profile method [27] using the WinPLOTR/Fullprof suite program [28].

Thermogravimetric analyses (TGA) were carried out under oxygen by a Pyris thermogravimeter (PerkinElmer, Waltham, MA, USA). The analyses were carried out at a heating/cooling rate of 10 °C min^{-1}.

High resolution transmission electron microscopy (HRTEM) and electron diffraction (ED) patterns were performed in a JEOL 300FEG. The samples were prepared by crushing the powders under n-butanol and dispersing it over copper grids covered with a holey carbon film. Scanning electron microscope (SEM) images and corresponding EDX spectra were obtained with a JEOL JSM 6335F microscope. Samples were mounted on SEM stubs using carbon adhesive and gold sputter-coated. The composition of the obtained materials was established by quantitative ICP-OES analyses in a Spectro ARCOS with axial optical interface and high fluoric acid resistant nebulization system. Three replicates of the sample were digested in HCl/HF solution and further treated in a microwave system up to 210 °C. Besides, local composition was estimated by semi-quantitative chemical analysis using energy dispersive X-ray spectroscopy (EDS) both in SEM and TEM microscopes, and XPS experiments.

XPS measurements were carried on pelletized samples on a Physical Electronics spectrometer (PHI Versa Probe II Scanning XPS Microprobe with monochromatic X-ray Al Kα radiation (100 μm, 100 W, 20 kV, 1486.6 eV) and a dual-beam charge neutralizer. The spectrometer was calibrated with Au $4f_{7/2}$, Ag $3d_{5/2}$ and Cu $2p_{3/2}$ photoelectron lines at 84.0, 368.2 and 932.7 eV, respectively. The Au $4f_{7/2}$ line was recorded with 0.73 eV FWHM at a binding energy (BE) of 84.0 eV, under a constant pass energy mode at 23.5 eV condition. XPS spectra were analyzed using PHI SmartSoft software and processed using MultiPak 9.3 package. The binding energy values for the measured spectra at different etching times were referenced to O 1 *s* signal at 529.8 eV. Recorded spectra were fitted using Gauss–Lorentz curves. Atomic concentration percentages of the constituent elements of the surfaces were determined taking into account the corresponding area sensitivity factor for the different measured spectral regions. Etching process was carried out using 1 kV Ar^+ bombardment of a 2 mm x 2 mm area. A sputter rate of 2.5 nm min^{-1} is assumed, as determined for SiO_2 under the same sputter conditions.

Raman scattering measurements were conducted on a Witec Alpha 300 System using 532 nm wavelength excitation. The spectrometer was calibrated with a reference single-crystal Si sample (Raman peak at 520.7 cm^{-1}). The spectral data were collected at room temperature in a backscattering configuration in the spectral range of 100–900 cm^{-1}, with a laser spot of ~1 μm and laser power of ~2 mW.

The electrical measurements were performed by pressing powders under 6 kbar, into pellets with 6 mm of diameter and ca. 1mm of thickness, and sintering them at three different temperatures: 800, 1100 and 1300 °C. The density of the pellets was estimated by the Archimedes method. For the a.c. electrical conductivity measurements, blocking electrodes were deposited on both sides of the as-pelletized samples by platinum paint (previously dried at 500 °C). The a.c. conductivity data were obtained, from −100 to 200 °C, with a frequency analyzer (Solartron 1260) coupled with a dielectric interface (Model 1296A) over a frequency range of 1–10^7 Hz, and under oscillation voltage of 600 mV. Resistance and permittivity values were derived from the complex impedance diagrams.

2.2. Synthesis of powders and preparation of pellets

The powder samples were prepared by the ceramic method starting from Nb_2O_5 (Merck, 99.9%) and $NaNO_3$ (Merck, 99.5%). The metal precursors were firstly treated at 400 °C for one day and at 600 °C for four days. After this, the samples were further treated at 800 °C for a day. At the end of each heat treatment the samples were quenched down to ambient temperature. From preliminary experiments, we observed that this procedure succeeded in preparing NN as pure samples, avoiding the stabilization of usual secondary phases such as $Na_2Nb_4O_{11}$. Typical white pellets of NN were prepared by mixing the corresponding powders with 5% wt. sodium alginate ($C_6H_7O_6Na$, from Sigma-Aldrich) as a binder and further pressing. For this purpose, water was added to the mix and then the suspension was stirred and smoothly heated up to dryness. Different pellets were then placed on a platinum sheet and sintered by additive treatments at 800 °C/1 d, 1100 °C/4 h and 1300 °C/2 h. These pellets were denoted as NN-800, NN-1100 and NN-1300, respectively. At these temperatures sodium alginate was totally decomposed, as deduced from TGA analysis (Fig. S1). In our experimental conditions, the use of this binder does not significantly affect the final composition of the pellets, within the experimental error. Besides, under oxygen atmosphere, neither a gain nor a loss of mass was observed in the cooling regime, pointing to the stabilization of the expected oxidation states for the different cations, i.e. Na^+ and Nb^{+5}.

The densification of the pellets was estimated from both SEM inspection and density measurements. Pycnometric measurements permitted to obtain the density of the pellets as follows: 4.07, 4.21 and 4.39 g/cm^3 for NN-800, NN-1100 and NN-1300, which represent relative density values of 89, 92 and 96%, respectively.

3. Results and discussion

3.1. Structural and compositional characterization

XRD data of the NN powders and pellets were refined by the Rietveld method [28]. As mentioned above, several symmetries and space groups have been previously proposed for describing $NaNbO_3$ at room temperature. Thus, orthorhombic nonpolar *Pbma* (called P, AFE phase) usually describes powder microcrystals and nanowires. Besides, doped, strained and small-sized samples, together with nanocubes have been described by the orthorhombic polar $P2_1ma$ (usually called Q, FE phase). In fact, the coexistence of both phases at room temperature is not rare [15]. The actual *Pbma* phase has been suggested to consist of three different phases, predominating a monoclinic *Pm* phase at room temperature [29]. As the electrical response of these ceramics is highly sensitive to their structure, different possibilities have been explored in the Rietveld refinements of the NN ceramics. From a preliminary inspection of certain angle regions (Fig. 1), the appearance of Bragg peaks at 2θ values of 36.6° and 55.2° could be appreciated. These maxima have been previously reported to correspond to the characteristic AFE superlattice peaks of the *Pbma* polymorph [5]. Nevertheless, a certain amount of the Q phase had to be considered because of several details such as the maximum appearing at 43.3° with considerable intensity, which is typical of $P2_1ma$ space group [7]. Hence, a refinement considering both polymorphs was chosen as the most reliable structural description of NN ceramics at room temperature. Fig. 1 shows the corresponding Rietveld profiles, obtaining a 69% of the P phase and a 31% of the Q phase. It is worth underlining that the XRD data provide mean macroscopic information with a maximum penetration depth (2θ = 90°) of ~40 and ~80 μm for the powder (packing ~0.6) and the pellets (packing ~0.9), respectively. In this sense, NN ceramic shows a mean structure well described by a mixture of the predominant AFE P polymorph and the Q phase in less extent. Nevertheless, the local stabilization of a mixture of other polymorphs must not be neglected. Besides, we had in mind that the XRD data on pellets can differ from those corresponding to powdered samples [30] due to strain effects, especially near the surface of the pellets. Thus, we refined the XRD data from NN-800 both in powder and in pellet forms, obtaining similar results.

As the sintering temperature is increased, diffraction maxima become narrower as expected. Besides, both P and Q phases remain present in the samples maxima typical of both polymorphs were observed regardless of the sintering temperature. Besides, relative percentage of Q phase decreases from 800 to 1300 °C sintering temperature, as pointed by the intensity of the maximum at 2θ = 43°, which is barely appreciable in NN-1300 ceramic (see Fig. 1a and b).

Complementarily, as Raman analysis is sensitive to different ionic environments, we performed several measurements at room temperature in order to complement the XRD results. Fig. 2 shows the Raman spectra of NN-800-powdered material collected in the range between 100 and 700 cm^{-1}, where the most important changes were observed. The spectra were de-convoluted in several components. The obtained main data and the corresponding assignment are summarized in Table 1. We observed the typical bands previously reported for the orthorhombic $NaNbO_3$ phase. At room temperature, Raman modes could be identified and deconvoluted in the wavenumber range 160–700 cm^{-1} [5,12,31]. This region is associated with internal vibrations of NbO_6 octahedral group. The signal at ~614 cm^{-1} was assigned to the A_{1g} mode. The signal undergoes shift at high vibrational frequency (~602-605 cm^{-1}) for $NaNbO_3$ [5,12,31], which can be attributed to sample preparation conditions. Lima et al. have reported that band A_{1g} (~600-612 cm^{-1}) and E_g (~556-561 cm^{-1}) at low temperatures (10–15 K) are well defined and are enlarged at temperatures above 200 K, coherently with our observations (Fig. 2a) [31]. Subtle differences in Raman spectra of the P and Q polymorphs have been previously reported, especially apparent in the range 100–300 cm^{-1} and also at high Raman shift values [5,13,15]. Thus, Fig. 2b–c gather the Raman spectra in selected wavelength ranges, showing the characteristic bands for the AFE and FE polymorphs, as reported previously [5,12,15,32]. Having this in mind, the spectra obtained by us are concordant with a mixture of predominant *Pbma* phase with $P2_1ma$ polymorph, in good agreement with XRD results commented above.

Mean macroscopic composition of the NN sample was obtained by ICP analyses. The average mass percentages were 9.0 ± 0.2 and 64.6 ± 1.5% for Na and Nb, respectively. Thus, the obtained data are concordant with the desired highly vacant-containing stoichiometry $Na_{0.56(2)}Nb_{1.00(1)}O_{2.8}$, i.e. the perovskite A-sublattice contains ~40% of vacancies. It has been previously stated that the presence of vacancies at the A sites in NN-doped systems as $Na_{1-x}Sr_{x/2}NbO_3$ can induce the stabilization of the Q phase at room temperature [33]. However, the A-sites deficiency in $Na_{1-x}NbO_3$ ceramics lead to more dense materials with smaller grain size and enhanced AFE distortion [19]. Therefore, the priority stabilization of one or another polymorph is probably connected to grain size and morphology considerations. The SEM inspection of the NN pellets, sintered at 800, 1100 and 1300 °C, showed interesting features, as can be appreciated in Fig. 3. For the acquisition of EDS spectra of whole grains at the pellets surface, ten regions for of each ceramic were typically analyzed and mean values were taken into account.

In the NN-800 pellet, two types of morphologies could be observed: intermediate-sized grains between 500 nm and 2 μm, and, in a smaller proportion, elongated rod-like formations of about 10 μm length. EDS analyses indicated an atomic composition of 0.87Na:1Nb (denoted with an A in Figs. 3c) and 0.43Na:1Nb (region B in Fig. 3c) for the grains and the bar-type formations, respectively. Mean values, taken from low magnification images (Fig. 3a), led to 0.57Na:1Nb. Previous works indicated that whereas coarse grains of more than 2 μm trend to stabilize into the *Pbma* phase, submicrometric grains show mostly the $P2_1ma$ polymorph [4,13]. On the other hand, hydrothermally prepared $NaNbO_3$ long-bars also crystallize in S. G. $P2_1ma$ [34]. In this sense, the NN-800 ceramic would consist of micrometric grains of *Pbma* phase

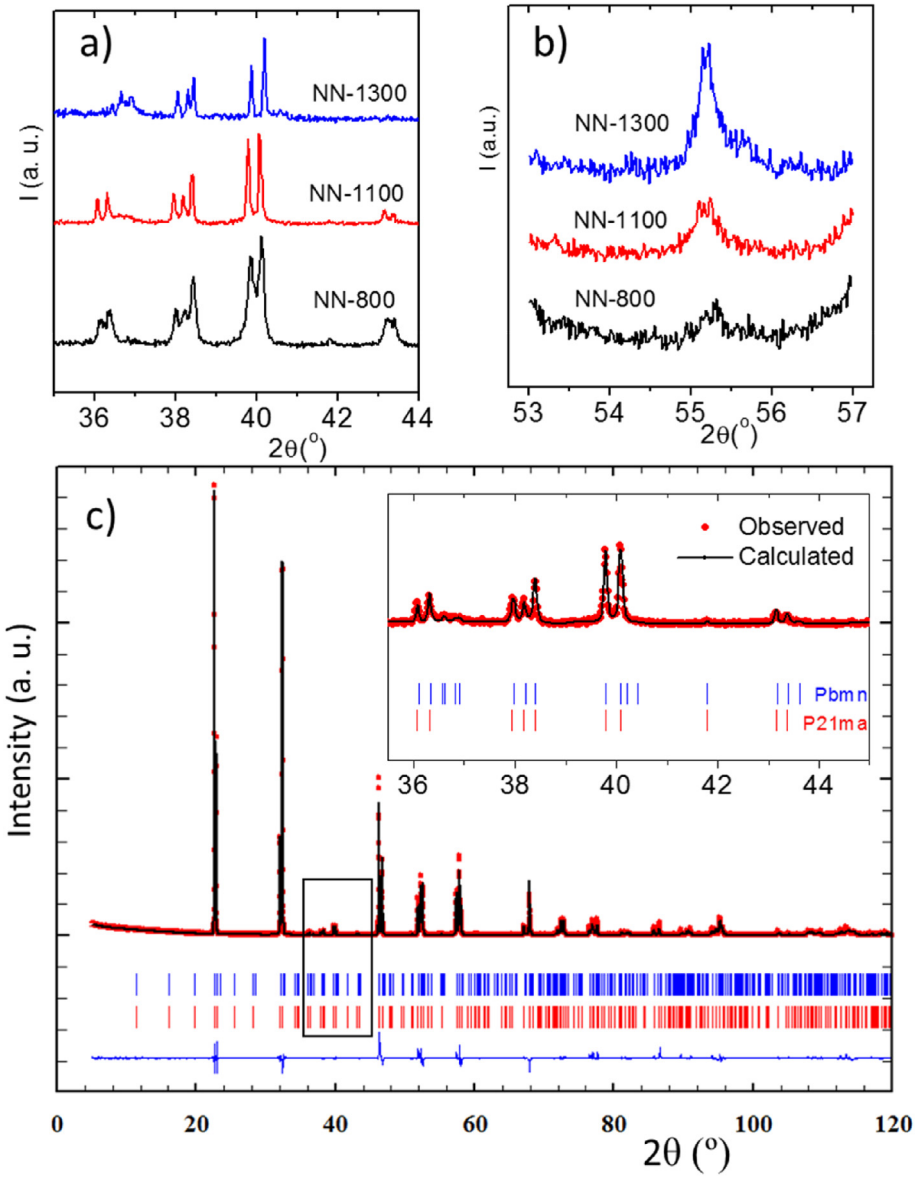

Fig. 1. XRD data for the NN-800, NN-1100 and NN-1300 pellets at a) and b) selected angle ranges showing the AFE superlattice peaks of the *Pbma* polymorph and the typical $P2_1ma$ reflection at ca. 43°; c) Rietveld profiles considering both phases for the NN-1100 pellet. Botton blue line refers to the difference between observed and calculated profiles. Inset shows a zoomed view of significant 2theta range. (For interpretation of the references to colour in this figure legend, the reader is referred to the Web version of this article.)

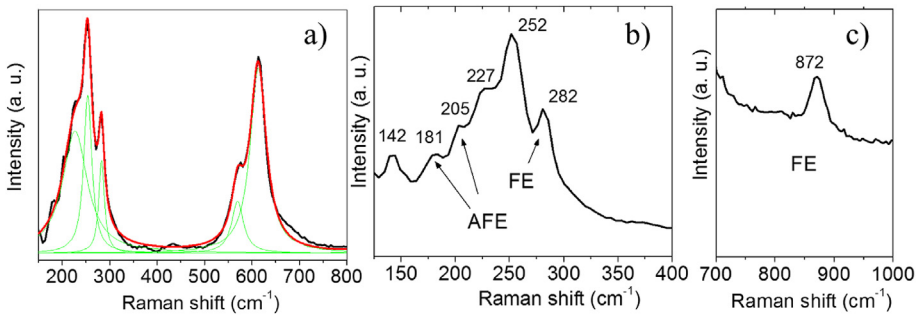

Fig. 2. Raman spectra NN powder sample a) with the different contributions as deduced from the fitting of the different peaks with Lorentzian curves (green lines) between 180 and 800 cm^{-1}, and b), c) selected region showing the bands belonging to AFE and FE phases. (For interpretation of the references to colour in this figure legend, the reader is referred to the Web version of this article.)

together with long bars formations mostly stabilized in the $P2_1ma$ polymorph. As sintering temperature is increased up to 1100 °C, these two morphologies evolve differently but the Na:Nb mean ratios obtained for NN-800 are maintained. Thus, the grains (0.40Na:1Nb) increase in size and become more homogeneous (region B in Fig. 3f), whereas the bar-type formations (0.54Na:1Nb) seem to melt easily during sintering process, giving rise to vitreous-like regions, denoted with an A in Fig. 3f. Mean EDS analyses from low magnification images gave an atomic composition ratio of 0.59Na:1Nb. Finally, for a sintering temperature of 1300 °C, well-sintered micro grains of size ranging

Table 1
Crystallographic data, R-factors from the Rietveld refinements, mean composition and Raman modes for the NN ceramics.

	NN-800	NN-1100	NN-1300
Pbma			
a (Å)	5.5683(1)	5.5714(2)	5.5685(9)
b (Å)	15.5394(4)	15.528(5)	15.527(1)
c (Å)	5.5164(1)	5.5113(2)	5.5045(4)
R_B	4.84	7.93	9.31
X^2	2.94	4.72	5.89
$P2_1ma$			
a (Å)	5.5741(1)	5.5754(1)	5.5690(9)
b (Å)	7.7646(1)	7.7607(2)	7.765(1)
c (Å)	5.5172(1)	5.5171(2)	5.506(1)
R_B	4.36	7.10	10.90
X^2	2.77	6.93	6.56
Mean composition[a]:		Raman modes (cm^{-1})/assignation	
ICP: $Na_{0.57(1)}Nb_{1.00(1)}O_{2.8}$		224.6/F_{2g} 254.6/F_{2u}	
XRD: $Na_{0.6(1)}Nb_{1.0(1)}O_{2.8}$		286.5/F_{2u} 569.3/E_g	
EDS: $Na_{0.59(3)}Nb_{1.00(1)}O_{2.8}$		614.1/A_{1g}	

[a] Cation concentrations were obtained from ICP measurements, refined occupations from XRD data and EDS data. Oxygen content was estimated by electroneutrality considerations.

between 2 and 15 μm are visible in the pellet surface, coherently with the estimated density values. Mean SEM analyses gave an atomic ratio 0.61Na:1Nb for NN-1300. A representative EDS spectrum is shown in Fig. 3i.

Therefore, the stabilization of a mixture of a majority P phase at room temperature in the NN ceramics is concordant with XRD, Raman and SEM results. In this way, we obtained mean compositions for NN very close to those obtained by ICP, within the experimental error (Table 1): $Na_{0.6}NbO_3$. The mean composition was practically the same for NN-800, NN-1100 and NN-1300. We further explored local composition and microstructural homogeneity of the ceramics by HRTEM/EDS and XPS analyses. Fig. 4a shows the typical aspect of a NN crystal, with a clear polydomain morphology [6], similar to that previously observed in annealed $BaTiO_3$ ceramics, i.e. domains uniaxially aligned inside the grains which disrupt near grain boundary regions [24]. In several frontiers a somewhat coalescence between several nanocrystals is observed, which show well developed interplanar distances. This domain-type microstructure has been previously related to the FE or AFE response in undoped and doped NN samples [6,14]. Moreover, it is well known that FE and AFE polymorphs can coexist over a wide temperature range, particularly in twined samples [12]. Besides, nanoregions in which different orientations of the present polymorphs develop could be appreciated in some crystals, as shown in Fig. 4b. In it, nanoareas showing distances of ~1.56 nm corresponding to P polymorph are visible. Besides, compositional heterogeneity from the grain border towards the interior concerning the Na:Nb ratio could be appreciated (Fig. 4c). Thus, the Na concentration is higher in the borders and progressively decreases as the grain interior is reached.

In order to check the compositional homogeneity at the surface, pseudodepth XPS measurements were conducted by Ar^+ ions bombardment of the NN-800 pellet. Fig. 5 shows the corresponding C 1*s*, O 1*s*, Nb 3*d* and Na 1*s* core level spectra for the sample without etching. The C 1*s* core level spectrum can be decomposed into three contributions at 285.0, 286.6 and 288.9 eV assigned to adventitious carbon, C–OH and carbonate, respectively. The O 1*s* core level spectrum is partially overlapped by the Na KLL Auger signal at high binding energy, and can be decomposed into three contributions at 529.8, 531.3 and 532.3 eV. The first and more intense contribution at 529.8 eV

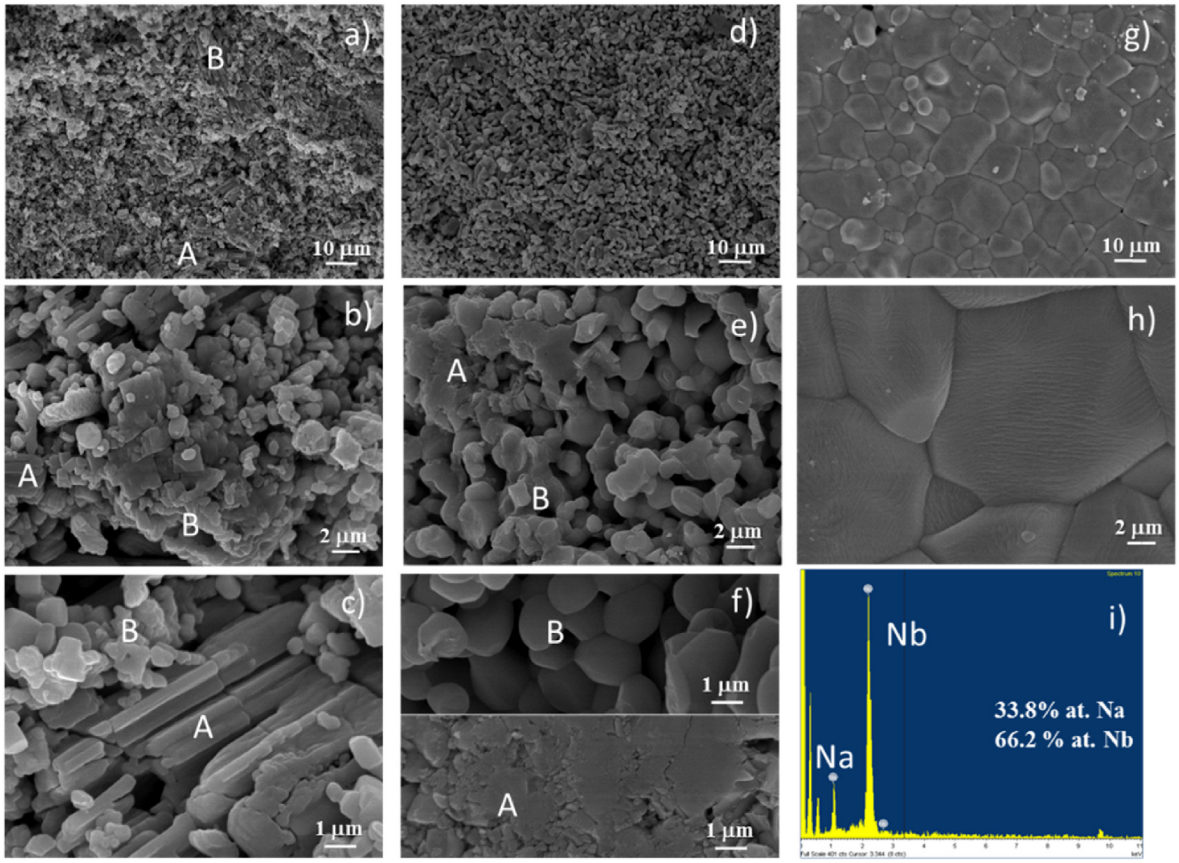

Fig. 3. Representative SEM images of the pellets at different magnifications for a), b), c) NN-800, d), e), f) NN-1100, g), h) NN-1300 and i) representative EDS spectra for NN pellets (NN-1100); line appearing at 0.525 keV corresponds to O and lines at 0.277 and 9.712 keV to C and Au, respectively (both employed for sample preparation).

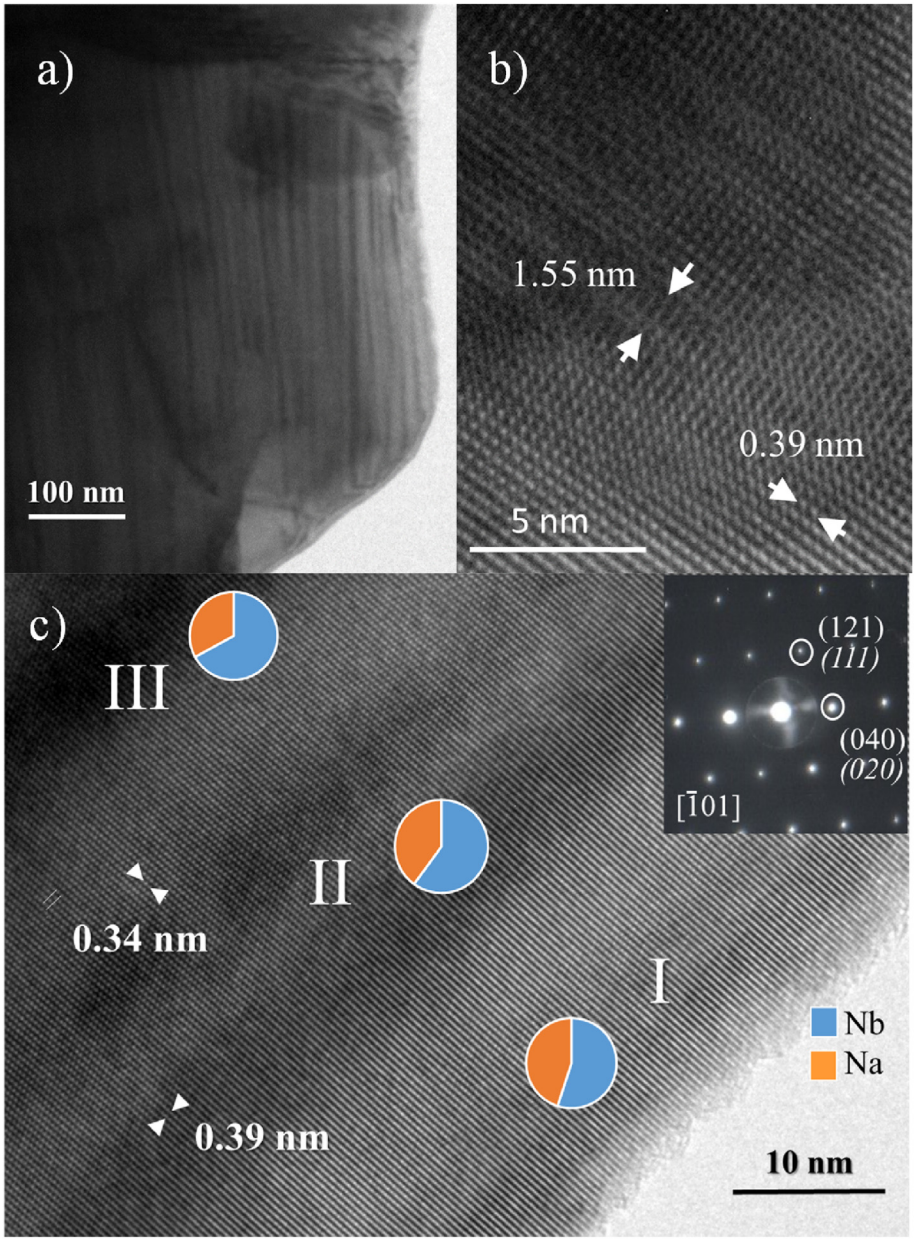

Fig. 4. HRTEM images at different magnifications showing a) polydomain morphology, b) domains between adjacent regions with different coherency and c) compositional segregation of Na from the interior to the grain border. Inset gathers the corresponding ED pattern; Miller indexes in italic refers to Q polymorph.

corresponds to the lattice oxygen of the sodium niobate. The two photoemissions at higher binding energy can be assigned to chemically nonequivalent neighborhood of the oxygen atoms derived from the occurrence of additional sodium species, as will be described later, and to changes in the crystallographic surrounding as previously observed Molak et al. [35]. The Nb 3*d* core level spectrum shows the doublet Nb $3d_{5/2}$ and Nb $3d_{3/2}$, with a Nb $3d_{5/2}$ at 206.8 eV, typical of Nb(V) for $NaNbO_3$. The Na 1*s* spectrum is asymmetric and can be decomposed into two contributions at 1071.2 and 1072.2 eV. The first one derived from Na(I) of the perovskite and the second one at high binding energy to other Na(I) segregated species with different conductivity such as surface carbonate or Na–O species [35].

Table 2 shows the surface chemical composition in atomic concentration % and the Na/Nb atomic ratio for sample NN-800 at different etching times with Ar^+ plasma. Hence, the evolution of the Na/Nb atomic ratio versus the etched time can be observed. The observed Na/Nb atomic ratio is higher than 1 due to the simultaneouspresence of sodium carbonate on the surface. Upon etching, as expected, the surface concentration of carbon decreased, and the C 1s core level spectrum (not shown) of the etched sample after 10 min does not show any contribution at high binding energy, and the Na/Nb atomic ratio decreased as going from the surface to the pellets inner part, pointing to a clear chemical segregation concerning Na cations, as observed in the HRTEM study (Fig. 4). This decrease in the Na/Nb atomic ratio was also observed by Molak et al. [35], when using different take off angles (15 and 45°). This accumulation of A-site cations at the surface is similar to that previously observed in the grain boundaries of an optimized commercial PTC ceramic, in which volatile Pb is more easily attracted to the highly strained grains borders [25].

3.2. Dielectric characterization

Electrical characterization of the NN pellets, sintered at different temperatures, was carried out from impedance measurements between

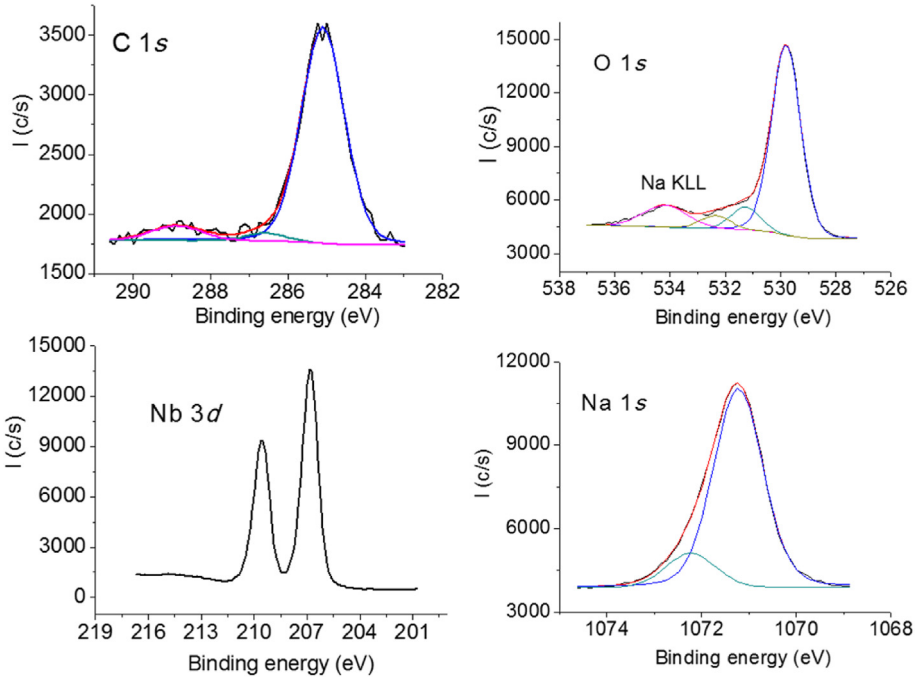

Fig. 5. C 1*s*, O 1*s*, Nb 3*d* and Na 1*s* core level spectra for sample NN-800.

Table 2
Surface chemical composition in atomic concentration % and the Na/Nb atomic ratio for sample NN-800 at different etching times with Ar^+ plasma.

Etched time with Ar^+ (min)	C 1*s*	Na 1*s*	Nb 3*d*	O 1*s*	Na/Nb atomic ratio
0	20.22	20.53	15.35	43.90	1.33
5	6.57	24.42	20.35	48.75	1.21
10	3.65	24.14	21.59	50.62	1.12

−50 and 200 °C and at frequencies varying from 1 Hz to 1 MHz. Typically, one flattened semicircle is obtained in the Z* Nyquist plots, in which bulk, grain boundary and electrode components are not well solved. For temperatures corresponding to lower resistance values, a tail appears at low frequencies. Representative Z* diagrams are depicted in Fig. S2.

Fig. 6 shows the variation of permittivity (ε') and dielectric losses (tgδ = ε''/ε') as a function of temperature for the NN-800, NN-1100 and NN-1300 ceramics at selected frequencies, at both heating and cooling regimes. In all cases, there are sharp dielectric peaks in the ε'vs T curves, both in the heating and the cooling processes. Though the ε' values experiment frequency dispersion, there is not a clear shift of the maxima temperatures at different frequencies, i.e. a clear relaxor-type behavior was not appreciated. The maxima appear at temperatures (T_C) of ca. 12 and −18 °C at the heating and cooling regimes, respectively. These maxima are accompanied by the correspondent dielectric anomalies in the tgδ vs T curves (see Fig. 6 b, d and f). An appreciable hysteretic behavior is therefore observed, corresponding to ΔT~ 30 °C, similarly to that previously reported for Ta-doped NN ceramics [36]. This hysteretic response has been related to the coexistence of boundaries of clearly different coherency between adjoining regions, pointing to the existence of a range of grain boundary potentials in the sample, as previously suggested for doped-$BaTiO_3$ ceramics [24]. The great dependence of the maxima height with the frequency, particularly intense in the heating curve, could indicate an interfacial Maxwell-Wagner-type polarization, which is accompanying the intrinsic behavior of the materials. Nevertheless, this behavior is maintained for the highly dense ceramic NN-1300, suggesting the intrinsic nature of the observed response, probably linked to phase transitions in the samples.

It is clear from literature that NN material experiments several dielectric anomalies as a function of temperature, connected to its temperature-driven structural transitions. However, the temperatures of the different transitions considerably vary for specimens with different stoichiometries, grain sizes and chemical dopants. Relevant data for selected materials from the literature are summarized in Table S1. The temperature of the P-R transition of $NaNbO_3$ can be shifted 140° to lower temperatures just doping with a 4% atomic of $CaHfO_3$. It is therefore plausible to consider than in our vacancy-containing NN samples the P-Q transition is reduced down to ~12 °C on heating and to ~ -18 °C on cooling. Besides, a hysteresis as high as 30° is also observed in our case, which is typical of heterogeneous/doped samples. P-phase could be related to Na-poor regions whereas Na-rich regions would predominantly correspond to the Q-phase [37].

Mishra demonstrated from high-resolution powder neutron diffraction data that the temperature ranges of stabilization for each NN polymorph do change in heating and cooling regimes [38], probably due to the different kinetics implied in the transformation between polymorphs. Thus, from kinetic considerations, it has been proposed that the different processes implied (AFE – FE transition) polarization in FE domains and FE – AFE transition have different energy barriers to overcome and hence different rates [16]. In this way, the hysteretic behavior in ε'vs T curves in heating and cooling regimes could be an effect of the diverse mechanisms implied and also a consequence of the different stability of NN polymorphs over the explored temperature ranges. The temperature of the maximum in ε' vs T shifts towards lower values in NN on cooling regime, coherently with previously reported results [3]. Certainly, FE and AFE polymorphs coexist in a wider temperature range when cooling than in the heating regime [38], giving rise to smearing effects in the dielectric behavior.

Fig. 7 depicts the frequency variation of the imaginary parts of dielectric modulus and impedance. A comparative inspection of both Z'' and M'' curves permits to analyze deeper the obtained response. The electric modulus ($M^* = 1/\varepsilon^*$) formalism was initially introduced [39] to study space charge relaxation phenomena, but it is currently widely used to complement the analysis of the impedance data. Whereas M* plots specially inform about elements with the smallest capacitance in the dielectric system, Z* formalism highlights those most resistive

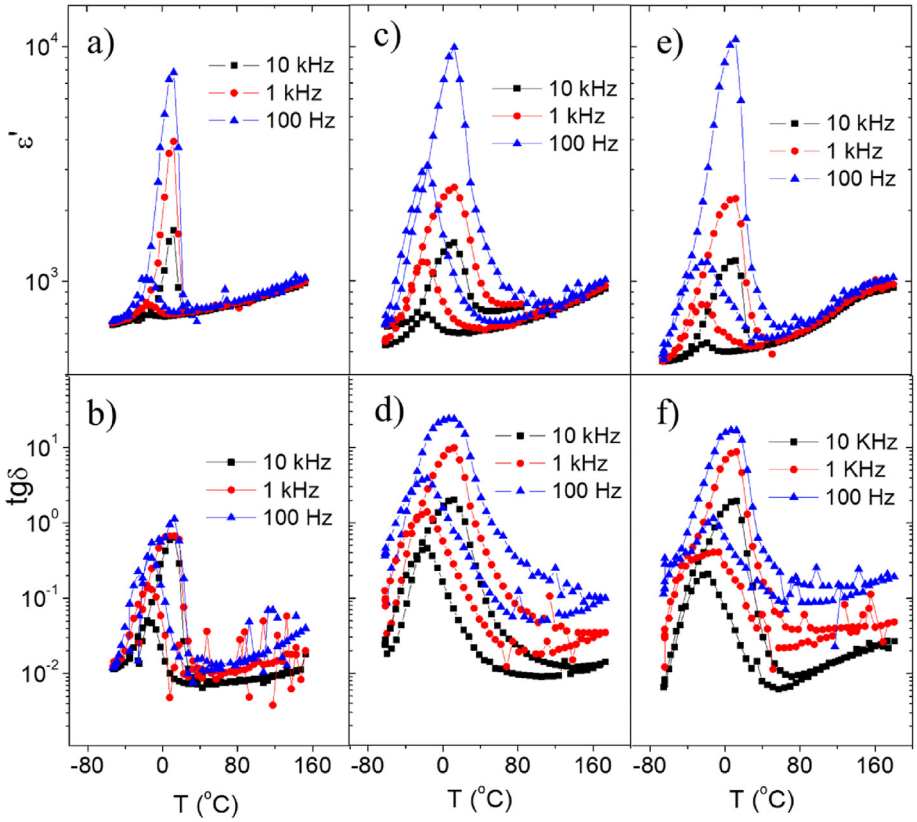

Fig. 6. Temperature dependence of ε' and tgδ at selected frequencies and at heating and cooling regimes for a), b) NN-800, c), d) NN-1100 and e), f) NN-1300, respectively.

elements. These curves, Z" and M" vs frequency, give relaxation Debye peaks which evolve with temperature, being $Z''_{max} = R/2$ and $M''_{max} = \varepsilon_o/2C$, the maxima M" and Z" values at each temperature.

It is worth underlining two interesting features of the curves shown in Fig. 7. First, both the Z" and M" maxima are shifted to higher frequencies as temperature increases up to around 5 °C. From ~6 to 20 °C, where the PTCR response is displayed, the peaks are practically not shifted at all. Finally, from 20 to 200 °C, they are shifted towards lower frequencies as the temperature increases. This behavior is similar to that displayed by PTCR $BaTiO_3$-based ceramics for temperatures below, near or above the switching one, T_C [40]. Second, the evolution in the intensity of both Z_{max}" and M_{max}" peaks also follows an opposite trend when heating up to T_C and heating from T_C. Thus, this evolution of Z" maxima suggests a PTCR behavior. The height of the M" maxima changes around the T_C observed in the ε'vs T curve and this is coherent with the presence of transitions implying AFE or FE phases [41]. Interestingly, above 20 °C the M" peaks are shifted to lower frequency values as temperature increases. This unusual behavior is actually the fingerprint of the PTCR behavior [42]. Thus, the evolution from low T to T_C is similar to that previously observed in AFE materials such as $Bi_2Ti_4O_{11}$ [41]. Besides, the observed trend above T_C in our case matches the usual response of FE materials above the transition [43]. This suggests the presence of both type of interactions in the NN samples, confirming the data from XRD and Raman spectroscopy.

Fig. 8 comparatively gathers in more detail the evolution of Z" and M" maxima at selected temperatures for NN-1300. Heating regime is shown in Fig. 8 as a representative example. Fig. S3 presents the corresponding curves for the cooling regime. The different maxima appearing in these curves reveal four electroactive components operating in the frequency window explored, indicated as 1, 2, 3, 4 in Fig. 8. Component 1 could be ascribed to electrode effects, operating at very low frequencies. Components 2 and 3 seem to be resistive-capacitive elements playing a crucial role in the electrical response of the materials. They both show capacity values between 80 and 100 pF. Besides,

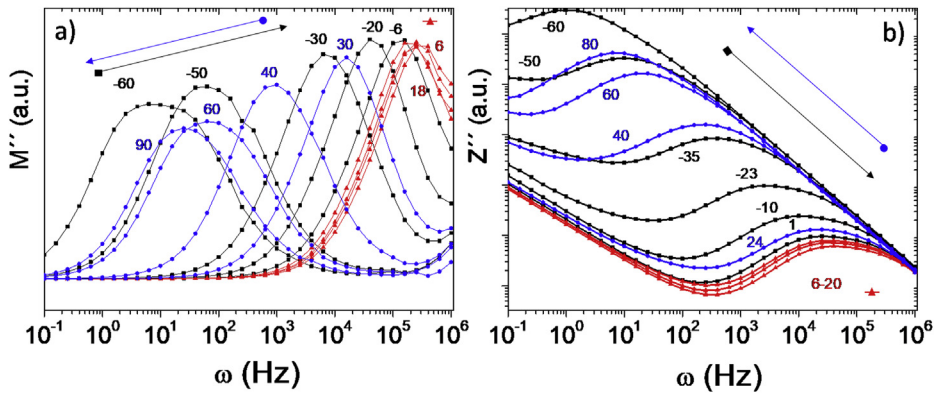

Fig. 7. Variation of imaginary parts of a) modulus and b) impedance (in logarithmic scale) vs frequency for NN-1300 at the heating regime. Numbers refer to temperature values in °C. Black squares, blue circles and red triangles serve as a guide to the eye for following the evolution of the curves. (For interpretation of the references to colour in this figure legend, the reader is referred to the Web version of this article.)

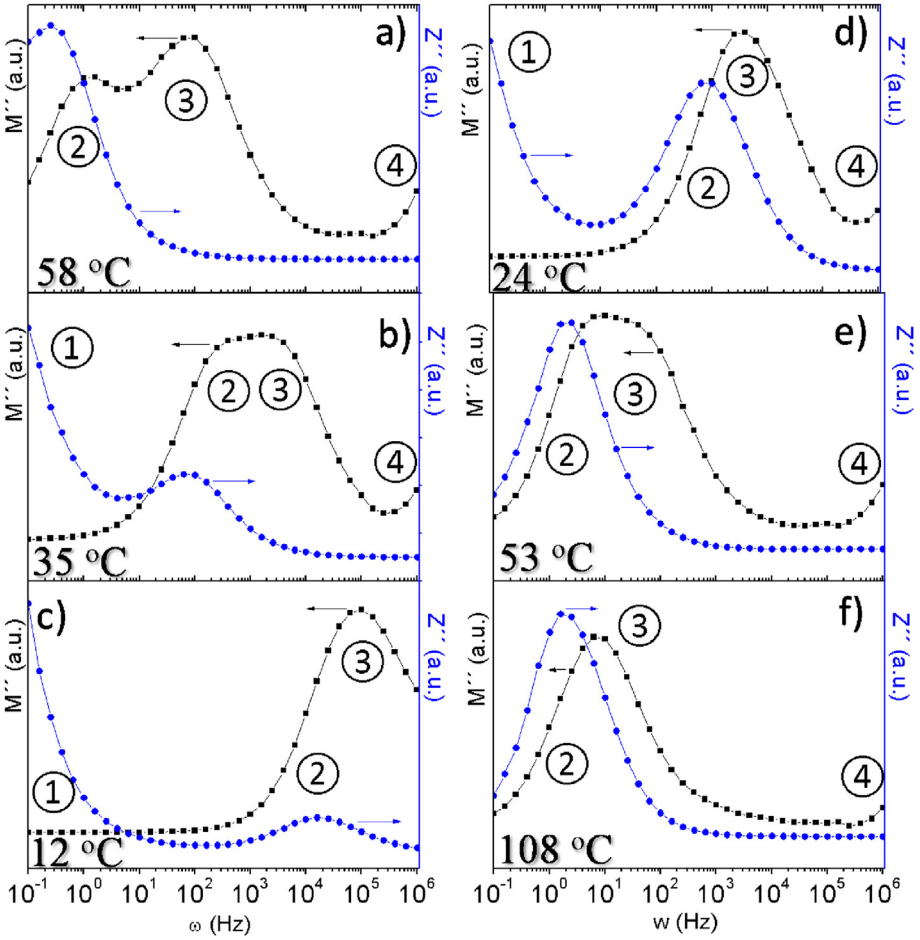

Fig. 8. Variation of M" and Z" vs frequency curves for NN-1300 on heating regime at selected temperatures. The numbers 1–4 refer to the different electroactive regions.

component 2 shows resistivity values ranging between 10^5 and 10^{10} Ω cm, whereas component 3 is clearly less resistive. Having in mind the compositional segregation operating in the NN pellets, components 2 and 3 could be interpreted considering two consecutive surface layers, the first one forming the grain boundaries. They collapse giving rise to a single broad peak as temperature approach the T_C. Near this temperature, both peaks are shifted to higher frequencies, suggesting that long range motion of carriers can take place at intermediate frequency values. These carriers probably consist of sodium vacancies. However, at temperatures far from the transition (Fig. 8 a and f) short range mobility is probably operating. Finally, component 4 could be related to bulk contribution, which falls out of the frequency window explored.

Ayvazian et al. have previously demonstrated that the grain boundaries are preferential conductive paths through a polycrystalline PTCR $BaTiO_3$ film [44]. Such type of domains of different orientation and/or symmetry have been widely observed previously in strontium-doped NN samples [33]. Moreover, it has been shown by atomic force microscopy on a commercial $BaTiO_3$ thermistor that two contributions are operating in PTCR ceramics: grain boundary regions between grains and outer-shell regions of each grain (which typically extend over a 10% of grains volume) [43,45]. Therefore, in our case the electrical response is plausibly mainly due to two electroactive surface layers developed in the samples as a consequence of compositional segregation. Indeed, the grain boundaries are usually related to excessive free volume and therefore atomic diffusion towards the inter-grains regions from the crystals bulk should be considered [46].

Fig. 9 shows the variation of resistivity with temperature for NN-800, NN-1100 and NN-1300 ceramics, in heating and cooling regimes. For NN-1300 the data of a second cycle is also included, showing well reproducibility of the measured data. This second cycle was carried out once the first cycle was finished, after leaving the sample inside the measurement-cell for 12h. The electrical response of the NN materials indeed suggests a PTCR thermistor behavior near room temperature. This effect is very large on heating regime though it is decreased in cooling cycle. Indeed, the coexistence of FE and AFE phases is more stable over temperature variations for twinned samples as the ours and, having in mind the substantial differences between both polymorphs, large hysteresis is not unexpected for the transition [12]. In fact, this hysteresis has been already observed and interpreted taking into account the difficulties in the structural changes needed and the stabilization of two phases in different temperatures ranges for the heating and cooling regimes [38].

At temperatures below the transition, the activation energy value of the process was estimated by applying an Arrhenius law from −60 to −30 °C. For NN-1300 in the heating regime, we obtained an activation energy value of E_a = 0.85 eV. This value around 1 eV probably corresponds to vacancies and ion transport processes. In this sense, compositional segregation could act as a chemical potential and vacancies/Na^+ migration seems to dominate up to a certain temperature value, in which compositional homogeneity is achieved. Through this process, AFE (P phase) to FE (Q phase) transition takes place leading to the observed maxima in ε'vs. T curves. This transition is probably concomitant with partial transitions to PE phases (e.g. R). Above T_C, symmetry is higher and the overlapping between *d* orbitals would become more effective, leading to an activated conduction process

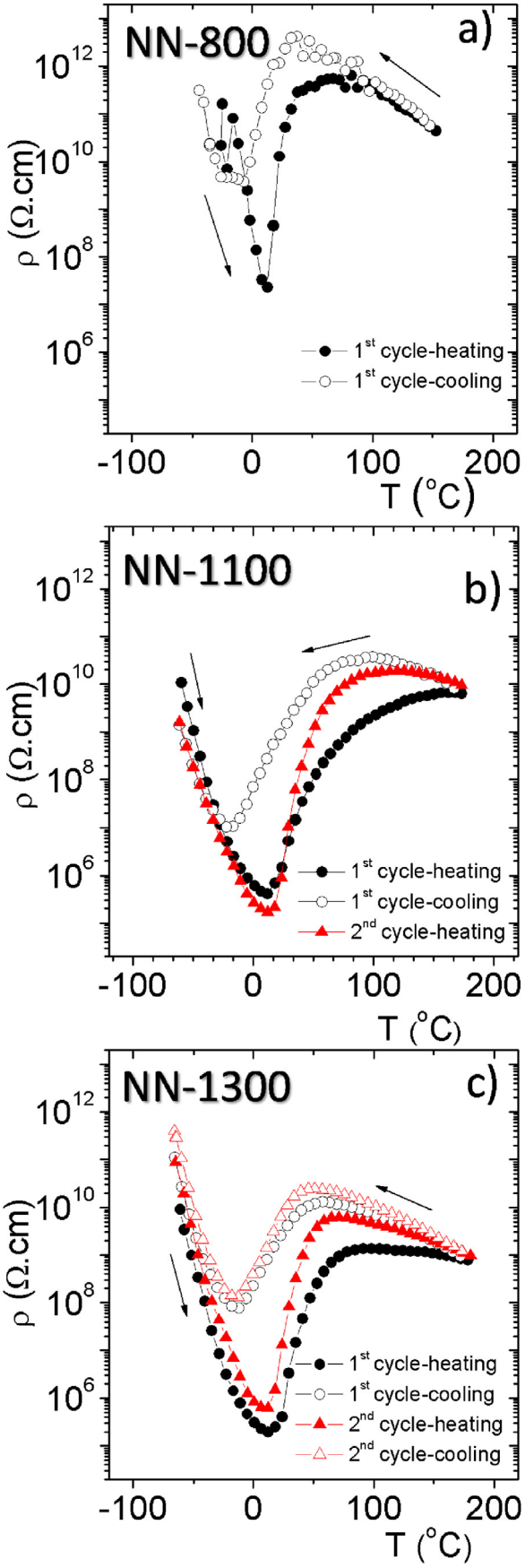

Fig. 9. Resistivity vs. temperature at heating and cooling regimes for a) NN-800, b) NN-1100 and c) NN-1300 (two cycles). Arrows indicate the heating and cooling curves.

probably implying other additional carriers [47].

Interestingly, previous density functional theory calculations in $BaTiO_3$ pointed directly to a FE-AFE model in order to explain the PTCR behavior. Thus, this behavior was interpreted as the result of competition between FE (low energy) and AFE (high entropy) couplings [48]. Therefore, the coexistence of AFE and FE interactions, together with the presence of high concentration of vacancies heterogeneously distributed, seem to be crucial in the PTCR behavior displayed by the NN electroceramics.

4. Conclusions

Highly A-site defective NN powders have been successfully prepared by ceramic method. Pelletized ceramics sinterized at 800, 1100 and 1300 °C showed relative density values of 89, 92 and 96%, respectively, as obtained from pycnometric measurements. ICP-OES measurements indicated a mean composition of $Na_{0.57(1)}Nb_{1.00(1)}O_{3-x}$, which is coherent with the EDX-SEM analyses of the materials.

The materials presented co-stabilization of the two phases commonly observed at room temperature in $NaNbO_3$-based materials, i.e. P and Q polymorphs, being predominant the antiferroelectric P phase (~70%). This result, deduced from Rietveld refinements of X-ray diffraction data, is coherent with the obtained Raman data.

SEM exploration showed two different particle morphologies, which evolve differently through partial melting as sintering temperature is increased. In the ceramic sintered at 1300 °C (NN-1300), well sintered micrograins were apparent. EDX analyses from HRTEM studies showed a significant compositional segregation concerning sodium cations. Hence, they are accumulated at the grains surface whereas the Na concentration decreases as going towards the grains interior.

The dielectric characterization of the NN ceramics was carried out by impedance spectroscopy measurements, between −100 and 200 °C. Maxima in ε'vs T curves were obtained at temperatures, T_C, around −12 and 18 °C, in heating and cooling regimes, respectively. These maxima are frequency-dependent but do not clearly show relaxor-type characteristics. Typical values of maximum permittivity and tangent loss at 10 kHz were around $\varepsilon' = 1250$ and $tg\delta = 2$, and $\varepsilon' = 65$ and $tg\delta = 0.04$, on heating and cooling regimes, respectively. Up to our knowledge, this dielectric anomaly implying high electrical polarization has not been observed before at such low temperatures. Besides, the analysis through modulus and impedance formalisms showed the fingertip characteristics of a positive-temperature-coefficient resistor (PTCR) response. Indeed, this type of response was clearly observed in the ρ vs. T curves, in which resistivity jumps of about three orders of magnitude were displayed. The PTCR behavior has been analyzed and interpreted considering two electroactive components, probably related to surface layers. A mechanism implying vacancy/cation motion has been proposed to operate at temperatures above T_C. Finally, the compositional segregation (shown by EDX and ICP data) and the coexistence of AFE and FE transitions seem to be the key features governing the observed electrical behavior in the NN ceramics.

Acknowledgments

The authors thank the CAIs of the UCM for facilities: XRD, ICP-OS, EM measurements; and also to FONDEQUIP grant EQM140142 for Raman Witec Alpha 300 equipment. This work was supported by Spanish MINECO (MAT2017-84118-C2-2-R Project), Ministerio de Ciencia, Innovación y Universidades (RTI2018-099668-BC22 Project), and Junta de Andalucía and FEDER (UMA18-FEDERJA-126 Project).

Appendix A. Supplementary data

Supplementary data to this article can be found online at https://doi.org/10.1016/j.ceramint.2020.03.253.

References

[1] P. Kumari, R. Rai, S. Sharma, M. Shandilya, A. Tiwari, State-of-the-art of lead free ferroelectrics: a critical review, Adv. Mater. Lett. 6 (6) (2015) 453, https://doi.org/10.5185/amlett.2015.4086.

[2] E.A. Wood, Polymorphism in potassium niobate, sodium niobate, and other ABO_3 compounds, Acta Crystallogr. 4 (1951) 353, https://doi.org/10.1107/S0365110X51001112.

[3] S.K. Mishra, N. Choudhury, S.L. Chaplot, P.S.R. Krishna, R. Mittal, Competing antiferroelectric and ferroelectric interactions in $NaNbO_3$: neutron diffraction and theoretical studies, Phys. Rev. B 76 (2007) 24110, https://doi.org/10.1103/PhysRevB.76.024110.

[4] J. Koruza, P. Groszewicz, H. Breitzke, G. Buntkowsky, T. Rojac, B. Malič, Grain-size induced FE in NaNbO3, Acta Mater. 126 (2017) 77, https://doi.org/10.1016/j.actamat.2016.12.049.

[5] S. Ji, H. Liu, Y. Sang, W. Liu, G. Yu, Y. Leng, Synthesis, structure, and piezoelectric properties of ferroelectric and antiferroelectric $NaNbO_3$ nanostructures, CrystEngComm 16 (2014) 7598, https://doi.org/10.1039/c4ce01116c.

[6] H. Shimizu, H. Guo, S.E. Reyes-Lillo, Y. Mizuno, K.M. Rabec, C.A. Randall, Lead-free antiferroelectric: $xCaZrO_3$-(1-x) $NaNbO_3$ system ($o < x < 0.1$), Dalton Trans. 44 (2015) 10763, https://doi.org/10.1039/C4DT03919J.

[7] G. Gouget, M. Duttine, E. Durand, A. Villesuzanne, V. Rodriguez, F. Adamietz, T. Le Mercier, M.D. Braidac, A. Demourgues, Isolating the two room-temperature polymorphs of NaNbO3: structural features, optical band gap and reactivity, ACS Appl. Electron. Mater. 1 (4) (2019) 513, https://doi.org/10.1021/acsaelm.8b00125.

[8] Q. Liu, L. Zhang, Y. Chai, W.L. Dai, Facile fabrication and mechanism of single-crystal sodium niobate photocatalyst: insight into the structure features influence on photocatalytic performance for H_2 evolution, J. Phys. Chem. C 121 (2017) 25898, https://doi.org/10.1021/acs.jpcc.7b08819.

[9] R. Barbosa-Silva, J.F. Silva, U. Rocha, C. Jacinto, C.B. de Araújo, Second-order nonlinearity of $NaNbO_3$ nanocrystals with orthorhombic crystalline structure, J. Lumin. 211 (2019) 121, https://doi.org/10.1016/j.jlumin.2019.03.012.

[10] H. Shi, X. Li, D. Wang, Y. Yuan, Z. Zou, J. Ye, $NaNbO_3$ nanostructures: facile synthesis, characterization, and their photocatalytic properties, Catal. Lett. 132 (2009) 205, https://doi.org/10.1007/s10562-009-0087-8.

[11] J. Qian, Y. Xue, Y. Ao, P. Wang, C. Wang, Hydrothermal synthesis of CeO_2/$NaNbO_3$ composites with enhanced photocatalytic performance, Chin. J. Catal. 39 (2018) 682, https://doi.org/10.1016/S1872-2067(17)62975-9.

[12] Z.X. Shen, X.B. Wang, M.H. Kuok, S.H. Tang, Raman scattering investigations of the antiferroelectric–ferroelectric phase transition of $NaNbO_3$, J. Raman Spectrosc. 29 (1998) 379, https://doi.org/10.1002/(SICI)1097-4555(199805)29:5<379::AID-JRS249>3.0.CO;2-F.

[13] Y. Shiratori, A. Magrez, J. Dornseiffer, F.H. Haegel, C. Pithan, R. Waser, Polymorphism in micro-, submicro-, and nanocrystalline $NaNbO_3$, J. Phys. Chem. B 109 (2005), https://doi.org/10.1021/jp052974p 20122.

[14] L. Gao, H. Guo, S. Zhang, C.A. Randall, A perovskite lead-free AFE $xCaHfO_3$-(1-x) $NaNbO_3$ with induced double hysteresis loops at room temperature, J. Appl. Phys. 120 (2016) 204102, https://doi.org/10.1063/1.4968790.

[15] Z. Liu, J. Lu, Y. Mao, P. Ren, H. Fan, Energy storage properties of $NaNbO_3$-$CaZrO_3$ ceramics with coexistence of ferroelectric and antiferroelectric phases, J. Eur. Ceram. Soc. 38 (2018) 4939, https://doi.org/10.1016/j.jeurceramsoc.2018.07.029.

[16] Y. Xu, W. Hong, Y. Feng, X. Tan, Antiferroelectricity induced by electric field in $NaNbO_3$-based lead-free ceramics, Appl. Phys. Lett. 104 (2014) 052903, , https://doi.org/10.1063/1.4863850.

[17] Y.-J. Hsiao, Y.-H. Chang, Y.-S. Chang, T.-H. Fang, Y.-L. Chai, G.-J. Chen, T.-W. Huang, Growth and characterization of $NaNbO_3$ synthesized using reaction-sintering method, Mater. Sci. Eng. B 136 (2007) 129, https://doi.org/10.1016/j.mseb.2006.09.013.

[18] T.A. Whittle, W.R. Brant, J.R. Hester, Q. Guc, S. Schmid, Tailoring phase transition temperatures in perovskites via A-site vacancy generation, Dalton Trans. 46 (2017) 7253, https://doi.org/10.1039/C7DT00352H.

[19] Y. Fan, Z. Zhou, R. Liang, M. Zhou, X. Dong, The effect of A-site nonstoichiometry on the microstructure and phase stability of $NaNbO_3$ polycrystalline ceramics, J. Eur. Ceram. Soc. 39 (2019) 4712, https://doi.org/10.1016/j.jeurceramsoc.2019.06.041.

[20] W.G. Mumme, I.E. Grey, B. Edward, C. Turner, J. Nino, T.A. Vanderah, $BiNb_3O_9$, a metastable perovskite phase with Bi/vacancy ordering:Crystal structure and dielectric properties, J. Solid State Chem. 200 (2013) 323, https://doi.org/10.1016/j.jssc.2013.01.05.

[21] A.P. Pivovarova, V.I. Strakhov, V.P. Popov, Phase relations in the $LaNb_3O_9$ – $NaNbO_3$ system in the temperature range of 20 to 800°C, Refract. Ind. Ceram. 42 (7 – 8) (2001) 285, https://doi.org/10.1023/A:1012718529213.

[22] M. Acosta, N. Novak, V. Rojas, S. Patel, R. Vaish, J. Koruza, G.A. Rossetti, J. Rödel, $BaTiO_3$-based piezoelectrics: fundamentals, current status, and perspectives, Appl. Phys. Rev. 4 (2017) 041305, , https://doi.org/10.1063/1.4990046.

[23] W. Heywang, Resistivity anomaly in doped barium titanate, J. Am. Ceram. Soc. 47 (10) (1964) 484, https://doi.org/10.1111/j.1151-2916.1964.tb13795.x.

[24] R.D. Roseman, N. Mukherjee, PCTR effect in $BaTiO_3$: structural aspects and grain boundary potentials, J. Electroceram. 10 (2) (2003) 117, https://doi.org/10.1023/A:1025647806757.

[25] K.M. Holsgrove, D.M. Kepaptsoglou, A.M. Douglas, Q.M. Ramasse, E. Prestat, S.J. Haigh, M.B. Ward, A. Kumar, J.M. Gregg, M. Arredondo, Mapping grain boundary heterogeneity at the nanoscale in a positive temperature coefficient of resistivity ceramic, Apl. Mater. 5 (2017) 066105, , https://doi.org/10.1063/1.4989396.

[26] Y. Saad, I. Álvarez-Serrano, M.L. López, M. Hidouri, Dielectric response and thermistor behavior of lead-free x $NaNbO_3$ - (1-x) $BiFeO_3$ electroceramics, Ceram. Int. 44 (2018) 18560, https://doi.org/10.1016/j.ceramint.2018.07.078.

[27] H.M. Rietveld, A profile refinement method for nuclear and magnetic structures, J. Appl. Crystallogr. 2 (1969) 65, https://doi.org/10.1107/S0021889869006558.

[28] J. Rodríguez - Carvajal, Recent advances in magnetic structure determination by neutron powder diffraction, J. Physiol. Biochem. 192 (1993) 55, https://doi.org/10.1016/0921-4526(93)90108-I.

[29] C.I. Cheon, H.W. Joo, K.-W. Chae, J.S. Kim, S.H. Lee, S. Torii, T. Kamiyama, Monoclinic ferroelectric $NaNbO_3$ at room temperature: crystal structure solved by using super high resolution neutron powder diffraction, Mater. Lett. 156 (2015) 214, https://doi.org/10.1016/j.matlet.2015.05.075.

[30] J. Koruza, J. Tellier, B. Malič, V. Bobnar, M. Kosec, Phase transitions of sodium niobate powder and ceramics, prepared by solid state synthesis, J. Appl. Phys. 108 (2010) 113509, https://doi.org/10.1063/1.3512980.

[31] R.J.C. Lima, P.T.C. Freire, J.M. Sasaki, A.P. Ayala, F.E.A. Melo, J. Mendes Filho, K.C. Serra, S. Lanfredi, M.H. Lente, J.A. Eiras, Temperature-dependent Raman scattering studies in $NaNbO_3$ ceramics, J. Raman Spectrosc. 33 (2002) 669, https://doi.org/10.1002/jrs.897.

[32] W. Li, X. Xia, J. Zeng, L. Zheng, G. Li, Significant differences in $NaNbO_3$ ceramics fabricated using Nb_2O_5 precursors with various crystal structures, Ceram. Int. 46 (2019) 3759, https://doi.org/10.1016/j.ceramint.2019.10.098.

[33] A. Torres-Pardo, R. Jiménez, J.M. González-Calbet, E. García-González, Room temperature ferroelectricity in $Na_{1-x}Sr_{x/2x/2}NbO_3$ through the introduction of cationic vacancies, J. Chem. Mater. 20 (22) (2008) 6957, https://doi.org/10.1021/cm802101r.

[34] D. Zhang, F. Shi, J. Cheng, X. Yang, E. Yan, M. Cao, Preparation and characterization of orthorhombic $NaNbO_3$ long bar, Ceram. Int. 40 (2014) 14279, https://doi.org/10.1016/j.ceramint.2014.06.018.

[35] A. Molak, M. Pawelczyk, J. Kubacki, K. Szot, Nano-scale chemical and structural segregation induced in surface layer of $NaNbO_3$ crystals with thermal treatment at oxidising conditions studied by XPS, AFM, XRD, and electric properties tests, Phase Transitions 82 (2009) 662–682, https://doi.org/10.1080/01411590903341155.

[36] J.J. Bian, M. Otonicar, M. Spreitzer, D. Vengust, D. Suvorov, Structural evolution, dielectric and energy storage properties of $Na(Nb_{1-x}Ta_x)O_3$ ceramics prepared by spark plasma sintering, J. Eur. Ceram. Soc. 39 (2019) 2339, https://doi.org/10.1016/j.jeurceramsoc.2019.02.007.

[37] R. Jiménez, M.L. Sanjuán, B. Jiménez, Stabilization of the ferroelectric phase and relaxor-like behaviour in low Li content sodium niobates, J. Phys. Condens. Matter 16 (2004) 7493, https://doi.org/10.1088/0953-8984/16/41/027.

[38] S.K. Mishra, R. Mittal, V. Yu Pomjakushin, S.L. Chaplot, Phase stability and structural temperature dependence in sodium niobate: a high-resolution powder neutron diffraction study, Phys. Rev. B 83 (2011) 134105, https://doi.org/10.1103/PhysRevB.83.134105.

[39] S.R. Elliott, C.T. Moynihan, R. Bose, Use of the modulus formalism in the analysis of ac conductivity data for ionic glasses, J. Non-Cryst. Solids 170 (1994) 97, https://doi.org/10.1016/0022-3093(94)90108-2.

[40] P.-H. Xiang, H. Takeda, T. Shiosaki, Characterization of manganese-doped $BaTiO_3$–$(Bi_{1/2}Na_{1/2})TiO_3$ positive temperature coefficient of resistivity ceramics using impedance spectroscopy, J. Appl. Phys. 103 (2008) 64102, https://doi.org/10.1063/1.2884714.

[41] J. Liu, Dielectric permittivity and electric modulus in $Bi_2Ti_4O_{11}$, J. Chem. Phys. 119 (5) (2003) 2812, https://doi.org/10.1063/1.1587685.

[42] Songwei Wang, Xin Zhang, Rong Yao, Liguo Fan, Huaiying Zhou, High-temperature dielectric relaxation behaviors in Mn_3O_4 polycrystals, Materials 12 (2019) 4026, https://doi.org/10.3390/ma12244026.

[43] D.C. Sinclair, A.R. West, Impedance and modulus spectroscopy of semiconducting $BaTiO_3$ showing positive temperature coefficient of resistance, J. Appl. Phys. 66 (8) (1989) 3850, https://doi.org/10.1063/1.344049.

[44] T. Ayvazian, G. Bersuker, Z.R. Lingley, M.J. Brodie, B.J. Foran, Conductive paths through polycrystalline $BaTiO_3$: Scanning probe microscopy study, Appl. Phys. Lett. 109 (2016) 072904, , https://doi.org/10.1063/1.4961443.

[45] P. Fiorenza, R. Lo Nigro, P. Delugas, V. Raineri, A.G. Mould, D.C. Sinclair, Direct imaging of the core-shell effect in positive temperature coefficient of resistance-$BaTiO_3$ ceramics, Appl. Phys. Lett. 95 (2009) 142904, https://doi.org/10.1063/1.3242418.

[46] Q. Yin, B. Zhu, H. Zeng, Microstructure, Property and Processing of Functional Ceramics, Springer-Verlag Berlin Heidelberg, 978-3-642-01694-3, 2010.

[47] D. Ihle, B. Lorenz, Small-polaron band versus hopping conduction in Fe_3O_4, J. Phys. C Solid State Phys. 18 (1985) L647, https://doi.org/10.1088/0022-3719/18/21/004.

[48] Q. Zhang, T. Cagin, W.A. Goddard III, The ferroelectric and cubic phases in $BaTiO_3$ ferroelectrics are also antiferroelectric, Proc. Natl. Acad. Sci. U.S.A. 103 (40) (2006) 14695, https://doi.org/10.1073/pnas.0606612103.